Activating Mobile Dislocation in Boron Carbide at Room Temperature via Al Doping

Jun Li, Kun Luo, and Qi An

Phys. Rev. Lett. **130**, 116104 — Published 15 March 2023

DOI: 10.1103/PhysRevLett.130.116104

Activating Mobile Dislocation in Boron Carbide at Room Temperature via Al Doping

Jun Li[1], Kun Luo[1], and Qi An[1,*]

[1]*Department of Materials Science and Engineering, Iowa State University, Ames, Iowa 50011, United States*

[*] Corresponding author-Email: qan@iastate.edu

Abstract

Dislocation glide, deformation twinning, and phase transition are critical mechanisms resulting in irreversible plastic deformations of materials. Due to the lack of dislocation movement, superhard ceramics generally exhibit brittle failure at room temperature. Here, by employing molecular dynamics simulations using a machine-learning force field, we reveal several plastic deformation mechanisms in superhard boron carbide as a small amount of aluminum (Al) is doped. Under shear deformation, dislocation nucleation and glide occur in Al-doped boron carbide (B_{12}-CAlC) due to the breakage of weakened chain bonds rather than the disintegration of icosahedral clusters. The dislocation activities then cause twin boundaries to migrate, thereby mitigating amorphization and enhancing ductility. Furthermore, the mobile dislocation with the Burgers vector of $\boldsymbol{b}=<1\bar{1}0>\{111\}$ is observed in the tensile nanopillar, which is well consistent with the experiment. This work demonstrates that mobile dislocation could be activated in superstrong covalent materials through a simple doping strategy.

The deformation mechanism of materials pertains strongly to the crystal structure, chemical composition, and bonding characteristics. Generally, metal alloys exhibit ductile deformation behaviors due to plastic deformation mechanisms including dislocation movement, deformation twinning, shear banding, and phase transformation [1,2]. In contrast, covalent or ionic solids often possess high strength yet exhibit brittle fractures with limited plasticity under ambient conditions, due to the strong chemical bonding [3,4]. Indeed, materials with dual properties of high strength and high ductility are very attractive for both scientific research and engineering applications. Eutectic high-entropy alloys with high strength and high ductility, for example, are excellent as-cast alloys for industrial equipment as propellers and adapters [5]. Therefore, it is desirable to improve the strength of metallic alloys and the ductility of covalent solids. Traditional methods for strengthening metallic materials involve the creation of internal precipitates and boundaries to obstruct dislocation movement [6,7], e.g. Hall-Petch relationship [8]. Whereas improving the ductility of covalent materials primarily relies on strategies like microalloying, grain boundary engineering, second-phase addition, etc. [9,10], which control the generation of internal defects and interactions between them (e.g. dislocation, stacking fault, and twinning), leading to plastic deformations [11].

Boron carbide is a prototype material for icosahedral solids, which exhibit very limited plastic deformation and abnormal brittle failure due to amorphous shear band formation [3,12,13]. These materials possess high hardness and low density, and they have been used in wide engineering

applications such as refractories, abrasives, and semiconductors [14-16]. Mitigating amorphization is pivotal to the design of boron carbide with improved ductility and mechanical performance for broader engineering applications. Many strategies have been proposed to suppress the amorphization of boron carbide, including doping [17], stoichiometry control [18], second-phase addition [19], and grain boundary engineering [20]. Quantum mechanics (QM) simulations suggested that the disintegration of icosahedra in boron carbide is triggered by strong interactions between chains and neighboring icosahedra, thereby causing amorphization [21,22]. Tailoring the chemistry of chains and icosahedra to reduce icosahedron-chain interactions has been suggested to mitigate amorphization and subsequently suppress the anomalous brittle failure in boron carbide. One effective approach to altering the chemistry of chains and icosahedra is doping foreign atoms. Recently, doping metallic atoms, such as Mg [23,24], Li [25,26], and Al [27], into boron carbide has become an attractive strategy to mitigate amorphization due to increased strength [26] or enhanced icosahedral rotation [23,27]. Interestingly, a recent experimental study displayed the presence of parallel dislocations in Al-doped boron carbide under indentation [27], suggesting these parallel dislocations may be formed from the same source. But there is no direct evidence showing that dislocations are mobile in these systems.

In the present study, several plastic deformation mechanisms are revealed in Al-doped boron carbide from machine-learning force field (ML-FF)-based molecular dynamics (MD) simulations. We find that Al doping activates mobile dislocations in boron carbide due to the breakage of

weakened chain bonds or icosahedral rotation. The mobile dislocations then cause stacking fault formation and twin boundary migration, thereby mitigating amorphization.

Boron carbide has a unique crystal structure composing of 12-atom (B_{12} or $B_{11}C^P$) icosahedra located at the vertices of a rhombohedral unit cell and a 3-atom C-B-C linear chain connecting icosahedra along the longest body diagonal (Fig. 1(a) and Fig. S1(a) [28]) [15]. Based on previous experiments and QM predictions [27,37], Al doping primarily modifies the C-B-C chain to the C-Al-C chain, leading to the most stable structure, B_{12}-CAlC (Fig. 1(b)). Similar to boron carbide, B_{12}-CAlC has complicated chemical bonding containing delocalized skeletal bonding within icosahedra and three-center-two-electron bonds among chains and icosahedra (Fig. 1(b) and Fig. S1(b) [28]), thus making it challenging to develop a classical force field for atomic interactions. Here, an ML-FF is developed by training deep neural networks based on atomic forces, system energies, and virial stresses derived from QM simulations [36]. The details of ML-FF development and validation are provided in Supplementary Material [28] and Fig. S2 [28].

With the developed ML-FF, we apply finite shear deformations on B_{12}-CAlC along several plausible slip systems: (001)/[100], (011)/[$2\bar{1}\bar{1}$], (111)/[$2\bar{1}\bar{1}$], (111)/[$\bar{1}\bar{1}2$], (111)/[$0\bar{1}1$], and (111)/[$\bar{1}10$], respectively, and compare its deformation behaviors with those of boron carbide (B_4C). Large supercells with the size of ~11.5 × 3.0 × 11.5 nm (43,200~51,840 atoms) are constructed by replicating the rotated unit cell along the slip system, in which the *x* direction is rotated to align with the slip direction, and the slip plane is in the *xy* plane of the Cartesian

coordinate system (Figs. 1(c)-(d) and Fig. S3 [28]). The details of MD simulations are discussed in Supplementary Material [28].

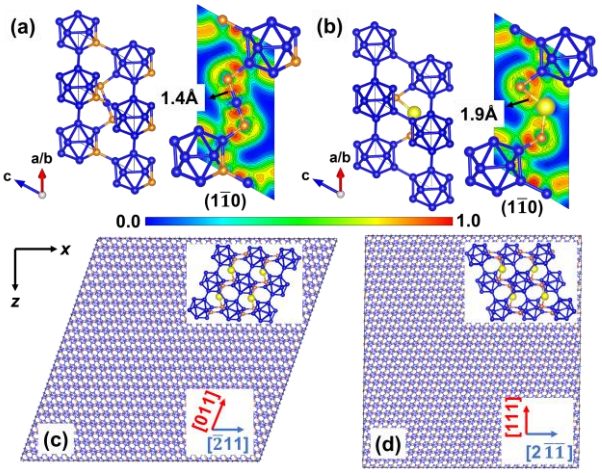

FIG. 1. The crystal structure and electron localization function of (a) B_4C and (b) B_{12}-CAlC, and the computational models of B_{12}-CAlC shearing along (c) (011)/[2$\bar{1}\bar{1}$] and (d) (111)/[2$\bar{1}\bar{1}$] slip systems. The blue, orange, and yellow balls represent B, C, and Al atoms, respectively.

The shear deformation behaviors of B_{12}-CAlC and B_4C are illustrated by the shear-stress-shear-strain relationships. As shown in Fig. S4 [28], B_4C exhibits brittle failure for all slip systems. Whereas Al doping significantly enhances ductility, and the critical failure strain of B_{12}-CAlC along the most plausible slip system reaches ~0.77, which is almost three times compared to that of B_4C. The shear strengths of B_{12}-CAlC along (001)/[100], (011)/[2$\bar{1}\bar{1}$], (111)/[2$\bar{1}\bar{1}$], (111)/[$\bar{1}\bar{1}$2], (111)/[0 $\bar{1}$ 1], and (111)/[$\bar{1}$ 10] slip systems are 20.0, 16.9, 16.9, 17.1, 20.6, and 20.7 GPa,

respectively, suggesting that (011)/[$2\bar{1}\bar{1}$], (111)/[$2\bar{1}\bar{1}$], (111)/[$\bar{1}\bar{1}2$] are three favorable slip systems for B_{12}-CAlC. In contrast to B_4C, B_{12}-CAlC exhibits various deformation behaviors after reaching the maximum shear stress, where an abrupt drop of stress occurs along (111)/[$\bar{1}\bar{1}2$], (111)/[$0\bar{1}1$], and (111)/[$\bar{1}10$] slip systems, while stress fluctuation/flow is observed along other slip systems. To explain the deformation behaviors, the snapshots and associated deformation mechanisms of B_{12}-CAlC along various slip systems are analyzed below.

The deformation processes of B_{12}-CAlC along the most plausible (011)/[$2\bar{1}\bar{1}$] slip system at 300 K are shown in Fig. 2 and Figs. S5-S7 [28]. Fig. 2 illustrates the nucleation and movement of dislocation, and the subsequent stacking fault formation. As the shear strain increases, C-Al chain bonds are first broken after elastic deformations, which causes Al atoms to be completely free from chains, providing favorable sites for dislocation nucleation (Fig. 2(a)). Then the dislocation glide is driven by shear strains due to the breakage of chain bonds, even at 300 K (Figs. 2(b)-(c)). The Burgers vector is identified as $\boldsymbol{b}$=<001>{100} or $\boldsymbol{b}$=<010>{100} for this partial mixed-type dislocation (Fig. 2(c)). Subsequently, the dislocation dipole with opposite Burgers vectors forms, moves towards each other, and eventually annihilates, leaving behind an imperfect crystal containing a stacking fault with one-icosahedral-layer twin boundaries (TBs) without fracturing icosahedra (Figs. 2(d)-(e)). Noteworthy, the twinned configuration of B_{12}-CAlC does not strictly obey the characteristic symmetry of twinned crystals, where only the icosahedra on the two sides of TBs form mutual mirror images. Then these TBs act as sources to initiate other dislocations of

the same type. The repetition of the dislocation initiation, glide, and following reaction near the TBs causes the TBs to migrate continuously during shear deformations and the shear stress to fluctuate (Fig. 2(a)), thereby mitigating amorphization. The details of TB migration caused by these dislocation activities are provided in Fig. S7 [28]. Particularly, the dislocation-TB interaction may cause strain hardening during shear deformations, thus strengthening B_{12}-CAlC (Fig. 2(a)). With further shear to the shear strain of ε=0.76686, a local amorphization region is formed in the twinned area due to the destruction of icosahedra, which then propagates and further develops into an amorphous band, indicating structural failure (Figs. S6(p)-(r) [28]). Similarly, TB migration is also observed in B_{12}-CAlC before amorphization for shear along the (001)/[100] slip system, leading the shear stress to fluctuate. However, this TB migration is caused by chain-bond-breakage-mediated icosahedral-layer slip rather than dislocation nucleation, glide, and annihilation. The detailed deformation processes along this slip system are provided in Figs. S8-S9 [28]. Overall, the ductility of boron carbide is significantly enhanced via Al doping due to TB migration, which is driven by the nucleation, glide, and reaction of partial dislocations parallel to the twin planes or by slippage of icosahedral layers.

The activated plastic deformation mechanisms involving mobile dislocation and TB migration in B_{12}-CAlC are attributed to the modification of crystal chemistry and bonding characteristics via Al doping. Since Al doping mainly alters the structure and bonding characteristics of chains, the length of chain bonds increases from 1.4 Å to 1.9 Å, and more

importantly, the bonds among chains and icosahedra change from two-center-two-electron bonds to weaker three-center-two-electron bonds (Figs. 1(a)-(b)). Thus, the weakened chain bonds act as sources to initiate the plastic deformation of B_{12}-CAlC, which is in stark contrast with that in undoped boron carbide, where the intra-icosahedra bonds break first due to interactions between chains and icosahedra (Fig. S10) [21,22]. Therefore, the dislocation nucleation and motion in B_{12}-CAlC are mainly attributed to the breakage of chain bonds resulting from the weakening effect via Al doping.

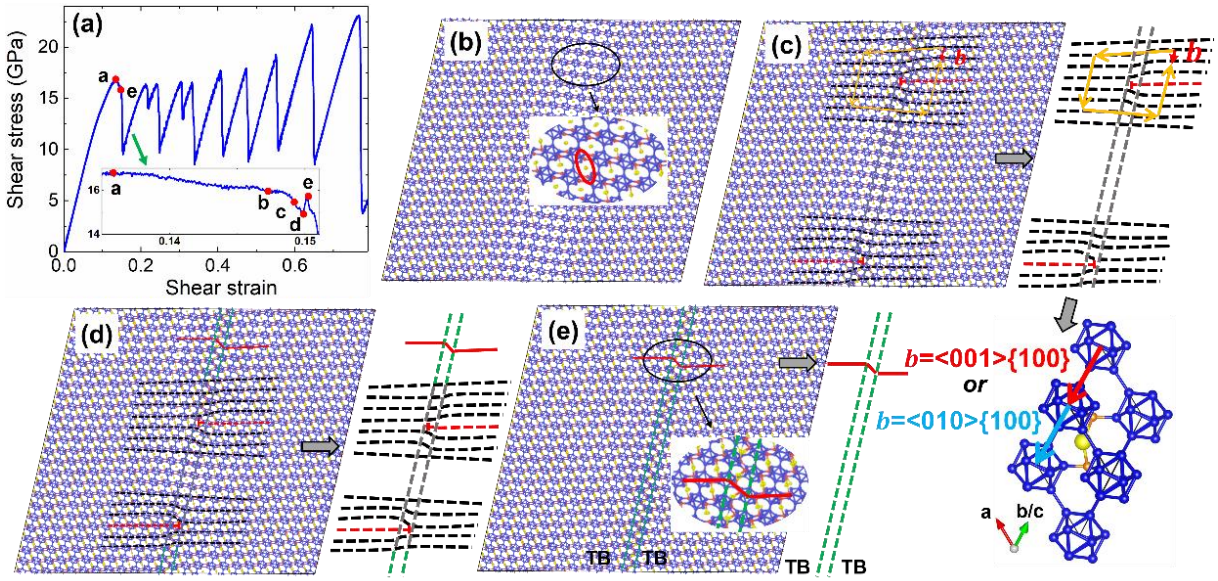

FIG. 2. (a) The shear-stress-shear-strain relationship, (b) dislocation nucleation due to the breakage of chain bonds, (c) and (d) partial dislocations movement with $\boldsymbol{b}$=<001>{100} or $\boldsymbol{b}$=<010>{100}, (e) dislocations reaction (annihilation), leaving behind a stacking fault, of B_{12}-CAlC along the (011)/[$2\bar{1}\bar{1}$] slip system at 300 K.

No TB migration is observed in B_{12}-CAlC shearing along other slip systems, although dislocation glide is indeed the main plastic deformation mechanism for the (111)/[$2\bar{1}\bar{1}$] and (111)/[$\bar{1}\bar{1}2$] slip systems. Fig. 3 and Figs. S11-S12 [28] illustrate the deformation processes of B_{12}-CAlC along the (111)/[$2\bar{1}\bar{1}$] slip system at 300 K. First, C-Al chain bonds are broken gradually after elastic deformations until most Al atoms are completely free from chains (Figs. 3(b)-(c)), causing the shear stress to just slightly decrease within a 0.09756 shear strain (Fig. 3(a)). The breakage of chain bonds causes icosahedral rotation (Fig. 3(d)). The rotation of icosahedral clusters is the source of the nucleation of dislocations. The generated partial dislocations with $\boldsymbol{b}$=<001>{010} or $\boldsymbol{b}$=<100>{010} form a dislocation dipole, which moves towards each other and eventually reacts and annihilates in amorphization or void regions, leaving behind stacking faults (Figs. 3(e)-(g)). Finally, the amorphization arising from disintegrated icosahedra propagates and merges to form an amorphous band, indicating structural failure (Figs. S12(h)-(i) [28]). When shearing along the (111)/[$\bar{1}\bar{1}2$] slip system, a similar mechanism is identified in B_{12}-CAlC by which dislocations nucleate by chain-bond-breakage resulting in icosahedral rotation, glide with $\boldsymbol{b}$=<100>{001} or $\boldsymbol{b}$=<010>{001} and finally annihilate in amorphization regions (Figs. S13-S14 [28]). Noteworthy, although the icosahedral rotation regions arising from the breakage of weakened chain bonds provide favorable sites for dislocation nucleation, these regions block dislocation movements, and thus TB migration and stress fluctuation are not observed in

(111)/[$2\bar{1}\bar{1}$] and (111)/[$\bar{1}\bar{1}2$] slip systems. There are no mobile dislocations in B_{12}-CAlC for (111)/[$0\bar{1}1$] and (111)/[$\bar{1}10$] slip systems. Instead, the breakage of weakened C-Al chain bonds mediates icosahedral-layer slip, which distorts and collapses some icosahedra, thereby causing amorphization in B_{12}-CAlC. The detailed deformation processes for these two slip systems are discussed in Figs. S15-S18 [28].

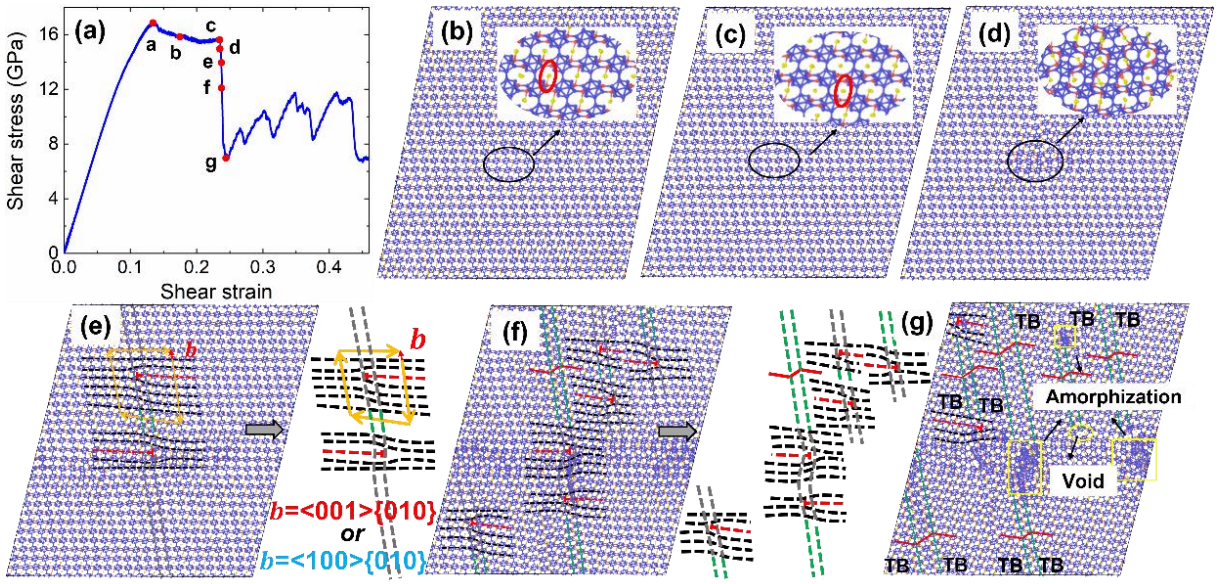

FIG. 3. (a) The shear-stress-shear-strain relationship, (b) and (c) the gradual breakage of chain bonds, (d) dislocation nucleation due to icosahedral rotation, (e) and (f) partial dislocations movement with ***b***=<001>{010} or ***b***=<100>{010}, (g) dislocations annihilation, of B_{12}-CAlC along the (111)/[$2\bar{1}\bar{1}$] slip system at 300 K.

Yang *et al* recently conducted indentation experiments on Al-doped boron carbide and

observed parallel dislocations with $\boldsymbol{b}=\langle 1\bar{1}0\rangle\{111\}$ near the crack tip using transmission electron microscopy, indicating the importance of the free surface in dislocation nucleation [27]. Therefore, we construct a B_{12}-CAlC nanopillar model, displayed in Fig. 4(a) and Fig. S19 [28], with a length-to-diameter ratio of ~1.5:1 (61,888 atoms), and conduct compression and tension along the $[\bar{5}77]$ direction that forms a ~45° angle with {111} plane in which dislocation slip may occur [27]. Fig. 4 and Figs. S20-S21 [28] display the tension process of the nanopillar, including the dislocation nucleation and its movement. As the tensile strain increases, B_{12}-CAlC deforms elastically, but the C-Al-C angles change suddenly, causing a small kink in the stress-strain relationship (Fig. 4(a)). The free surface acts as a source for dislocation nucleation, emitting a dislocation at the surface of the nanopillar due to the breakage of C-Al chain bonds and inter-icosahedral B-B bonds without fracturing icosahedra (Fig. 4(b)). The dislocation glides along the slip plane (Figs. 4(c)-(d)) and eventually annihilates at the surface. The Burgers vector for this perfect dislocation is $\boldsymbol{b}=\langle 1\,\bar{1}\,0\rangle\{111\}$, which matches experimental observations [27] and validates the present predictions. Finally, a cavity is formed near the surface and propagates along the slip plane, which further develops into a crack (Figs. S21(g)-(h) [28]). In contrast, when the B_{12}-CAlC nanopillar is under compression, the icosahedra are disintegrated along with icosahedral-layer slip and icosahedral rotation, thereby forming an amorphous shear band in the {111} plane (Figs. S22-S23 [28]).

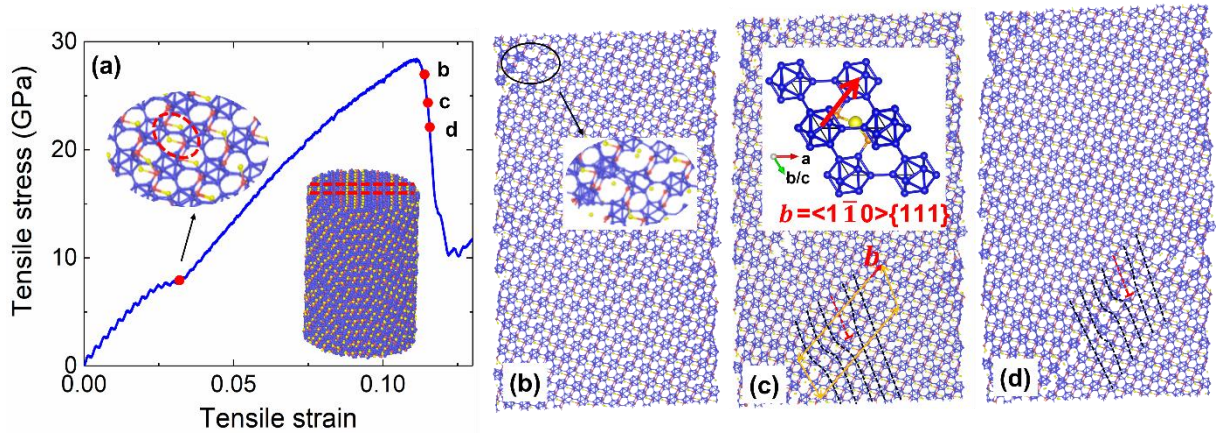

FIG. 4. (a) The tensile-stress-tensile-strain relationship, (b) dislocation nucleation due to the breakage of chain bonds and inter-icosahedral bonds near the surface, (c) and (d) perfect dislocation movement with $\boldsymbol{b}=\langle 1\bar{1}0\rangle\{111\}$, along the $[\bar{5}77]$ direction of the B_{12}-CAlC nanopillar at 300 K.

In summary, the ML-FF MD simulations indicate that tailoring the chain structure of boron carbide via Al doping can effectively activate mobile dislocations at room temperature. Al doping bends the linear chain of boron carbide and weakens its strong covalent bonding, making chain bonds relatively prone to breaking compared to the icosahedral bonds. For the most plausible $(011)/[2\bar{1}\bar{1}]$ slip system, the breakage of weakened chain bonds facilitates the nucleation and motion of partial dislocations, leading TBs to migrate, thereby mitigating amorphization and enhancing ductility. TB migration is also observed in the (001)/[100] slip system, which instead results from chain-bond-breakage-mediated icosahedral-layer slip. While for $(111)/[2\bar{1}\bar{1}]$ and $(111)/[\bar{1}\bar{1}2]$ slip systems, the breakage of weakened chain bonds induces icosahedral rotation,

which facilitates dislocation nucleation but blocks dislocation movement and further TB migration. A perfect dislocation is nucleated at the free surface of the B_{12}-CAlC nanopillar under tension, which glides with the Burgers vector of $\boldsymbol{b}=<1\bar{1}0>\{111\}$ and eventually annihilates at the surface. These findings signify that doping is an effective strategy to tailor deformation mechanisms in boron carbide, which provides a significant approach for mitigating amorphization and enhancing ductility and damage resistance in brittle ceramics.

Acknowledgement

This work was supported by NSF (CMMI-1727428).

References

[1] M. Chen, E. Ma, K. J. Hemker, H. Sheng, Y. Wang, and X. Cheng, Science **300**, 1275 (2003).

[2] J. Li, H. Chen, Q. Fang, C. Jiang, Y. Liu, and K. Liaw, Int. J. Plast. **133**, 102819 (2020).

[3] M. Chen, J. W. McCauley, and K. J. Hemker, Science **299**, 1563 (2003).

[4] S. Zhao, R. Flanagan, E. N. Hahn, B. Kad, B. A. Remington, C. E. Wehrenberg, R. Cauble, K. More, and M. A. Meyers, Acta Mater. **158**, 206 (2018).

[5] Y. Lu, Y. Dong, H. Jiang, Z. Wang, Z. Cao, S. Guo, T. Wang, T. Li, and P. K. Liaw, Scr. Mater. **187**, 202 (2020).

[6] M. Dao, L.Lu, R. J. Asaro, J. T. M. De Hosson, and E.Ma, Acta Mater. **55**, 4041 (2007).

[7] K. Lu, L. Lu, and S. Suresh, Science **324**, 349 (2009).

[8] N. Hansen, Scr. Mater. **51**, 801 (2004).

[9] J. Karch, R. Birringer, and H. Gleiter, Nature **330**, 556 (1987).

[10] B. R. Lawn, N. P. Padture, H. Cai, and F. Guiberteau, Science **263**, 1114 (1994).

[11] L. Porz, A. J. Klomp, X. Fang, N. Li, C. Yildirim, C. Detlefs, E. Bruder, M. Höfling, W. Rheinheimer, E. A. Patterson, P. Gao, K. Durst, A. Nakamura, K. Albe, H. Simons, J. Rödel, and L. Porz, Mater. Horizons **8**, 1528 (2021).

[12] J. Li, S. Xu, L. S. Liu, Z. Wang, J. Y. Zhang, and Q. W. Liu, Mater. Res. Express. **5**, 055204 (2018).

[13] J. Li and Q. An, J. Eur. Ceram. Soc. **43**, 208 (2023).

[14] J. Li and Q. An, J. Am. Ceram. Soc. **105**, 6826 (2022).

[15] J. Li, L. S. Liu, S. Xu, J. Y. Zhang, and Y. L. Wu, Materials. **11**, 1861 (2018).

[16] J. Li, S. Xu, J. Y. Zhang, L. S. Liu, Q. W. Liu, W. C. She, and Z. Y. Fu, Chinese Phys. B **26**, 047101 (2017).

[17] J. Li, S. Xu, J. Zhang, and L. Liu, J. Phys. Chem. C **125**, 11591 (2021).

[18] A. Chauhan, M. C. Schaefer, R. A. Haber, and K. J. Hemker, Acta Mater. **181**, 207 (2019).

[19] K. Y. Xie, K. Kuwelkar, R. A. Haber, J. C. LaSalvia, K. J. Hemker, and R. Hay, J. Am. Ceram. Soc. **99**, 2834 (2016).

[20] Y. Shen, M. Y. Yang, W. A. Goddard, and Q. An, J. Am. Ceram. Soc. **105**, 2978 (2022).

[21] Q. An, W. Goddard, and T. Cheng, Phys. Rev. Lett. **113**, 095501 (2014).

[22] J. Li, Q. An, and L. Liu, Phys. Rev. B **104**, 134105 (2021).

[23] B. Tang, Y. He, W. A. Goddard, and Q. An, J. Am. Ceram. Soc. **102**, 5514 (2019).

[24] S. Ando, N. Ishida, N. Kitamura, and Y. Idemoto, J. Am. Chem. Soc. **132**, 3968 (2016).

[25] H. Hillebrecht, N. Vojteer, V. Sagawe, K. Hofmann, and B. Albert, Zeitschrift Fur Anorg. Und Allg. Chemie **645**, 362 (2019).

[26] Y. He, Y. Shen, B. Tang, and Q. An, J. Am. Ceram. Soc. **103**, 2012 (2020).

[27] Q. Yang, C. J. Marvel, Y. Shen, M. He, J. Du, C. Hwang, E. D. Gronske, K. Y. Xie, S. R. Mercuio, Q. An, M. P. Harmer, K. J. Hemker, and R. A. Haber, Acta Mater. **241**, 118412 (2022).

[28] See Supplementary Material [url] for: (i) the calculation details of quantum mechanics simulations, development of machine-learning force field (ML-FF), validation of the ML-FF, and molecular dynamics simulations with the ML-FF; (ii) Fig. S1 displays the crystal structure and electron localization function of boron carbide (B_4C) and Al-doped boron carbide (B_{12}-CAlC); (iii) Fig. S2 displays the loss function and the root-mean-square-error of energy, force, and virial stress for both the training data and validation data; (iv) Fig. S3 displays the computational models of B_{12}-CAlC for shear deformations; (v) Fig. S4 displays the shear-stress-shear-strain relationships of B_{12}-CAlC and B_4C along (001)/[100], (011)/$[2\bar{1}\bar{1}]$, (111)/$[2\bar{1}\bar{1}]$, (111)/$[\bar{1}\bar{1}2]$, (111)/$[0\bar{1}1]$, and (111)/$[\bar{1}10]$ slip systems at 300 K; (vi) Fig. S5 displays the shear-stress-shear-strain relationship

of B_{12}-CAlC shearing along the (011)/[$2\bar{1}\bar{1}$] slip systems at 300 K; (vii) Fig. S6 displays the detailed deformation process of B_{12}-CAlC shearing along the (011)/[$2\bar{1}\bar{1}$] slip systems at 300 K; (viii) Fig. S7 displays the detailed deformation process of B_{12}-CAlC in the shear strain ranging from 0.24 to 0.25 shearing along the (011)/[$2\bar{1}\bar{1}$] slip systems at 300 K; (ix) Fig. S8 displays the shear-stress-shear-strain relationship of B_{12}-CAlC shearing along the (001)/[100] slip systems at 300 K; (x) Fig. S9 displays the detailed deformation process of B_{12}-CAlC shearing along the (001)/[100] slip systems at 300 K; (xi) Fig. S10 displays the shear-stress-shear-strain relationship and detailed deformation process of B_4C shearing along the (111)/[$\bar{1}\bar{1}$2] slip system at 300 K; (xii) Fig. S11 displays the shear-stress-shear-strain relationship of B_{12}-CAlC shearing along the (111)/[$2\bar{1}\bar{1}$] slip systems at 300 K; (xiii) Fig. S12 displays the detailed deformation process of B_{12}-CAlC shearing along the (111)/[$2\bar{1}\bar{1}$] slip systems at 300 K; (xiv) Fig. S13 displays the shear-stress-shear-strain relationship of B_{12}-CAlC shearing along the (111)/[$\bar{1}\bar{1}$2] slip systems at 300 K; (xv) Fig. S14 displays the detailed deformation process of B_{12}-CAlC shearing along the (111)/[$\bar{1}\bar{1}$2] slip systems at 300 K; (xvi) Fig. S15 displays the shear-stress-shear-strain relationship of B_{12}-CAlC shearing along the (111)/[$0\bar{1}$1] slip systems at 300 K; (xvii) Fig. S16 displays the detailed deformation process of B_{12}-CAlC shearing along the (111)/[$0\bar{1}$1] slip systems at 300 K; (xviii) Fig. S17 displays the shear-stress-shear-strain relationship of B_{12}-CAlC shearing along the (111)/[$\bar{1}$10] slip systems at 300 K; (xix) Fig. S18 displays the detailed deformation process of B_{12}-CAlC shearing along the (111)/[$\bar{1}$10] slip systems at 300 K; (xx) Fig. S19 displays the computational

model of B_{12}-CAlC nanopillar under compression and tension; (xxi) Fig. S20 displays the tensile-stress-tensile-strain relationship of the B_{12}-CAlC nanopillar along the [$\bar{5}$77] direction; (xxii) Fig. S21 displays the detailed tension process of the B_{12}-CAlC nanopillar along the [$\bar{5}$77] direction; (xxiii) Fig. S22 displays the compressive-stress-compressive-strain relationship of the B_{12}-CAlC nanopillar along the [$\bar{5}$77] direction; (xxiv) Fig. S23 displays the detailed compression process of the B_{12}-CAlC nanopillar along the [$\bar{5}$77] direction. which includes Refs. [14,21,22,27,29-39].

[29] G. Kresse, Phys. Rev. B **59**, 1758 (1999).

[30] G. Kresse and J. Furthmüller, Comput. Mater. Sci. **6**, 15 (1996).

[31] G. Kresse and J. Furthmüller, Phys. Rev. B **54**, 11169 (1996).

[32] P. E. Blöchl, Phys. Rev. B **50**, 17953 (1994).

[33] J. P. Perdew, K. Burke, and M. Ernzerhof, Phys. Rev. Lett. **77**, 3865 (1996).

[34] P. E. Blöchl, O. Jepsen, and O. K. Andersen, Phys. Rev. B **49**, 16223 (1994).

[35] R. Hill, Proc. Phys. Soc., London, Sect. A 349−354 (1952).

[36] H. Wang, L. Zhang, J. Han, and W. E, Comput. Phys. Commun. **228**, 178 (2018).

[37] Q. An, Phys. Rev. Mater. **5**, 103602 (2021).

[38] Q. An and W. A. Goddard, Chem. Mater. **27**, 2855 (2015).

[39] Q. An and W. A. Goddard, Phys. Rev. Lett. **115**, 095501 (2015).